

DEUTSCHES ELEKTRONEN-SYNCHROTRON
Ein Forschungszentrum der Helmholtz-Gemeinschaft



DESY 20-125
arXiv:2007.12639
July 2020

Controlled Density-Downramp Injection in a Beam-Driven Plasma Wakefield Accelerator

A. Knetsch et al.

ISSN 0418-9833

NOTKESTRASSE 85 - 22607 HAMBURG

DESY behält sich alle Rechte für den Fall der Schutzrechtserteilung und für die wirtschaftliche Verwertung der in diesem Bericht enthaltenen Informationen vor.

DESY reserves all rights for commercial use of information included in this report, especially in case of filing application for or grant of patents.

To be sure that your reports and preprints are promptly included in the
HEP literature database
send them to (if possible by air mail):

<p>DESY Zentralbibliothek Notkestraße 85 22607 Hamburg Germany</p>	<p>DESY Bibliothek Platanenallee 6 15738 Zeuthen Germany</p>
--	--

Controlled density-downramp injection in a beam-driven plasma wakefield accelerator

A. Knetsch,^{1,*} B. Sheeran,^{1,2} L. Boulton,^{1,3,4} P. Niknejadi,¹ K. Pöder,¹ L. Schaper,¹ M. Zeng,¹ S. Bohlen,^{1,2} G. Boyle,¹ T. Brümmer,¹ J. Chappell,⁵ R. D'Arcy,¹ S. Diederichs,^{1,2} B. Foster,⁶ M. J. Garland,¹ P. Gonzalez Caminal,^{1,2} B. Hidding,^{3,4} V. Libov,¹ C. A. Lindstrøm,¹ A. Martinez de la Ossa,¹ M. Meisel,^{1,2} T. Parikh,¹ B. Schmidt,¹ S. Schröder,^{1,2} G. Tauscher,^{1,2} S. Wesch,¹ P. Winkler,^{1,2} J. Wood,¹ and J. Osterhoff¹

¹Deutsches Elektronen-Synchrotron DESY, Hamburg, Germany

²University of Hamburg, Hamburg, Germany

³SUPA, Department of Physics, University of Strathclyde, Glasgow, UK

⁴The Cockcroft Institute, Daresbury, UK

⁵University College London, London, UK

⁶John Adams Institute for Accelerator Science at University of Oxford, Oxford, UK

(Dated: August 11, 2020)

This paper describes the utilization of beam-driven plasma wakefield acceleration to implement a high-quality plasma cathode via density-downramp injection in a short injector stage at the FLASHFORWARD facility at DESY. Electron beams with charge of up to 105 pC and energy spread of a few percent were accelerated by a tunable effective accelerating field of up to 2.7 GV/m. The plasma cathode was operated drift-free with very high injection efficiency. Sources of jitter, the emittance and divergence of the resulting beam were investigated and modelled, as were strategies for performance improvements that would further increase the wide-ranging applications for a plasma cathode with the demonstrated operational stability.

I. INTRODUCTION

Plasma wakes excited by charged particle beams [1–3] are capable of generating GV/m accelerating gradients [4, 5]. This is 2–3 orders of magnitude larger than conventional radio-frequency-based technologies, thereby promising a drastic reduction in both the size and cost of particle-accelerator facilities. Such a decrease is of particular significance for future linear colliders [6] and the provision of compact free-electron laser (FEL) photon sources. The research field of beam-driven plasma-wakefield accelerators (PWFA) is dynamic, with advances ranging from the energy doubling of a 42 GeV electron beam over less than a meter [7], to the controlled correction of a correlated energy spread within a plasma channel of tens of millimeters [8–10]. In particular, there has been significant progress in energy transfer from the beam driving the wake (the drive beam) to the trailing beam experiencing the accelerating field (the witness beam) [11–13]. Witness beams can be injected into the plasma wakefield either from an external source or internally by the trapping of ambient plasma electrons. Research on external injection methods has predominantly concentrated on maximizing energy transfer from the drive to the witness beam while preserving other beam parameters, such as emittance and energy spread [14, 15]. Internal injection methods with extremely high electric-field gradients (GV/m) have the potential to generate beams with exceptionally high quality. As opposed to injecting a beam into an accelerating structure, in these methods, a relativistic electron beam with much smaller phase space is formed directly

inside the accelerating structure. The predicted witness beams have normalized transverse emittance values much smaller than their drive beams and charges in the range of tens to hundreds of picocoulombs with femtosecond bunch durations [16–18]. Internal injection therefore offers the opportunity to generate a new class of beams with significantly enhanced brightness in comparison to conventional accelerator sources – an extremely desirable feature for future photon sources and applications in high-energy physics. While a variety of complementary internal injection methods have been shown to work in principle [19–21], precise control over the injection process, and consequently the injected witness-beam parameters, has so far remained relatively unexplored. This paper describes experiments carried out at FLASHFORWARD [22, 23] – a dedicated plasma-wakefield beamline adjacent to the FLASH facility [24], which operates with kiloampere-level beam currents and FEL-grade stability and beam quality [25]. It reports on the experimental demonstration of stable and controlled internal injection in PWFA utilizing a laser induced density downramp [26–29] and demonstrates for the first time a plasma cathode that can be reliably operated. The injected bunch properties as a function of laser alignment and laser energy are also explored.

II. DENSITY DOWNRAMP INJECTION

Generation of high-quality electron beams in a plasma accelerator via internal injection requires the trapping of electrons in the accelerating phase of the plasma wake. These electron populations can originate from within the wake through ionization injection [16, 18, 19, 30, 31] or from plasma electrons forming the boundary of the wake's ion cavity [26, 32]. Trapping will occur when

* alexander.knetsch@desy.de

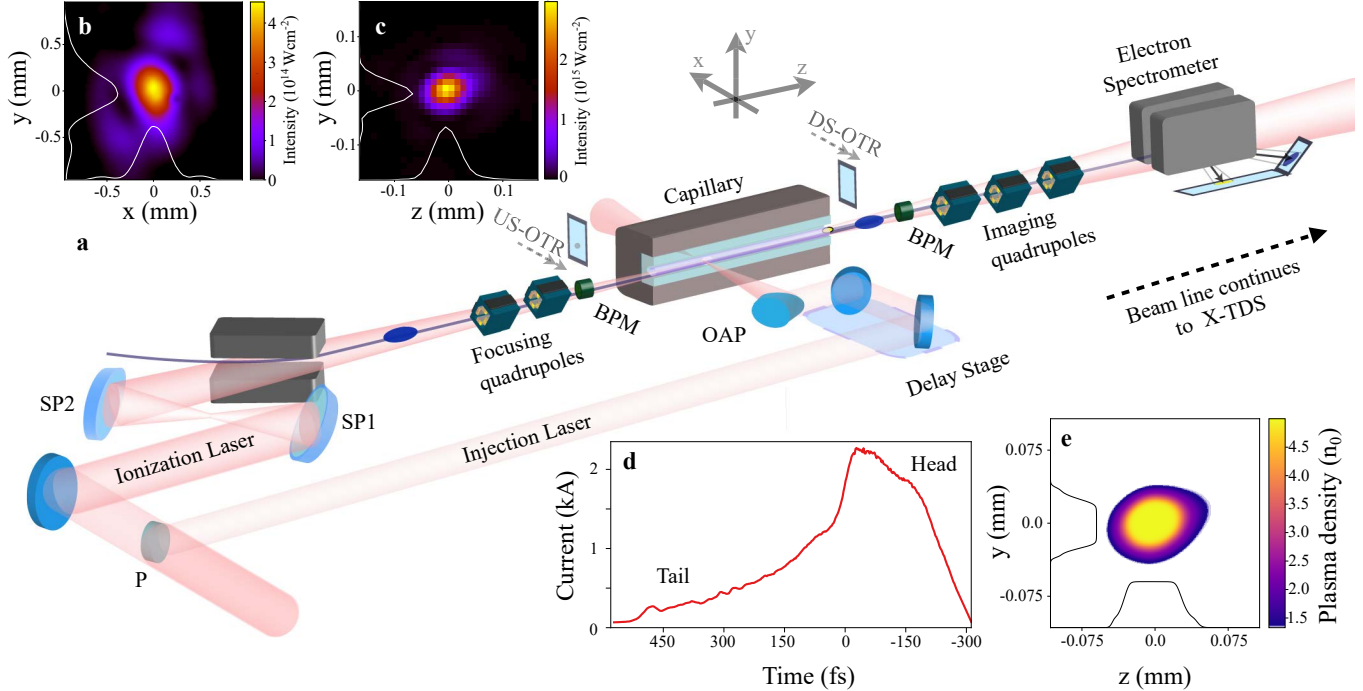


Figure 1. Schematic layout depicting the key elements of the experimental setup at FLASHFORWARD. (a) Laser and electron beamline layout: P is the pick-off mirror for the transverse injection laser beam, SP1 and SP2 are spherical mirrors focusing the longitudinal ionization laser and OAP is the off-axis parabola focusing the injection laser. The e-beam position monitors (BPM) are shown; US-OTR and DS-OTR represent the upstream and downstream optical-transition-radiation screens, respectively. These can be moved into the beam path as alignment diagnostics. Foci for the (b) ionization and (c) injection lasers on the US-OTR are shown. A side view of the plasma density calculated in the injection region from (c) is displayed in (d) (normalized to the background plasma density n_e). Black lines in (d) and white lines in (b,c) are axial projections. (e) is the measured current profile of the drive beam.

electrons that enter the accelerating phase of the plasma wake reach or exceed the phase velocity of the wake itself ($v_e \geq v_\phi$). Therefore, electrons need either to enter the wakefield at sufficiently high velocity or the potential of the plasma wake needs to be deep enough to accelerate these electrons to v_ϕ . The velocity of the plasma electrons depends on the strength of the generated wakefield which in turn is related to the drive beam and plasma densities. In a plasma of constant density, n_e , the phase velocity is equal to the velocity of the relativistic drive beam v_d , i.e., close to that of light, c . Such a stringent condition readily precludes trapping of electrons from the plasma background unless the phase velocity can be locally reduced using a plasma-density gradient [27, 33, 34]. A plasma density that decreases along the direction of propagation of the driver leads to a longitudinal expansion of the plasma wake with a concurrently reduced phase velocity of

$$v_\phi = v_d \left(\frac{1}{2n_e} \frac{\partial n_e(z)}{\partial z} \xi + 1 \right)^{-1}, \quad (1)$$

where $\xi = z - ct$ is the longitudinal coordinate in the co-moving frame, z is the longitudinal coordinate in the laboratory frame and t is time. As illustrated by Eq. 1,

the phase velocity on a density downramp decreases towards the back of the plasma wake, allowing fast plasma electrons to rephase into the accelerating region, where they eventually become trapped and can form a witness beam. If trapping is avoided except on the density downramp, the injection process can be controlled and density-downramp injection characterised in detail.

Numerical studies with 3D particle-in-cell (PIC) codes predict that density-downramp injection with a sufficiently sharp gradient produces electron beams with transverse normalized emittances below $1 \mu\text{m}$ [35–38]. Such sharp density downramps can be achieved either hydrodynamically, as commonly used in laser-driven plasma wakefield acceleration [39–41], or by ionization of distinct gas species with two perpendicularly focused laser arms [28, 29]; the latter is the approach pursued in this work.

III. EXPERIMENTAL SETUP

The experimental setup at FLASHFORWARD is depicted in Fig. 1. Electron beams with $\sim 800 \text{ pC}$ of charge reaching a mean energy of up to 1.25 GeV in the FLASH

linear accelerator were used to drive a wake inside a capillary plasma source. The plasma was created by ionization inside the capillary using two laser pulses – one focused along the electron-beam axis, the other transverse to it. Combined laser ionization thus formed a sharp density spike surrounded by a plateau region. Spatial alignment and synchronization were achieved with screens sensitive to optical transition radiation (OTR) and by measuring the plasma response due to beam-induced heating.

A. The plasma source

Constant-gas-flow capillaries have demonstrated excellent performance in plasma accelerators [39, 42, 43], allowing for tailored, short injector stages. For this experiment, a constant-flow capillary with a total length of 50 mm at a diameter of 1.5 mm with two gas inlets was designed. The capillary incorporates an additional access port with 300 μm diameter, used to couple in the transverse laser and located 20 mm downstream of the entrance, leaving a total maximum acceleration length of 30 mm for the injected witness beam. Gas-flow simulations performed with COMSOL Multiphysics [44] show that the transverse port reduces the plateau gas density by less than 2% and therefore has a negligible effect on the gas-density profile. Either pure argon, pure helium, or an arbitrary ratio of the two gases could be prepared in a mixing volume outside the central vacuum chamber before filling the capillary. In the experiments described in this work, the partial-pressure ratio between helium and argon was set to 2:1. Turbomolecular pumps were connected to the chamber to protect the beamline vacuum, reducing the ambient gas pressure by 3 to 4 orders of magnitude with respect to the pressure inside the capillary. A differential pumping system further reduced the pressure by 3 orders of magnitude both upstream and downstream of the central vacuum chamber. This design ensured that the quality of neither the drive nor witness beam was degraded by interfaces between vacuum chambers and scattering on ambient gas particles.

B. Laser ionization

The gas mixture was ionized by two independently focused arms of a 25 TW Ti:sapphire laser system synchronized to the FLASH electron beam at the 100-femtosecond level [45]. A 0.5' pick-off mirror inserted into the laser path reflected the central part of the 34 mm-diameter laser beam into the injection laser beamline. As depicted in Fig. 1(a), the remaining part of the laser continued to propagate along the ionization laser arm. A FWHM pulse duration of (40 ± 3) fs was measured in the injection laser beamline using optimized spectral properties for a short pulse at the injection laser focus. Focusing of the ionization laser was achieved by two spherical

mirrors with a resulting effective focal length of 18 m. Such a large effective focal length produced a focal spot with a FWHM in the x, y -direction of $(333 \times 461)\mu\text{m}$ (Fig. 1(b)). As a result, the Rayleigh range of the spot approached the meter scale with an intensity profile capable of ionizing a plasma column sufficiently long and wide enough to span the entire length of the capillary whilst fully containing the plasma wake. An $f/51$ off-axis parabola focused the injection laser perpendicular to the electron beam axis through a fused silica window. To minimize non-linear dispersion that can deteriorate the quality of the focal spot or pulse length, the window thickness was chosen to be 1.5 mm only. Since the gas profile at the transverse port was assumed to be flat, the resulting plasma-density shape from ionization was defined by the gas-mixture ratio and the injection-laser focus with a FWHM spot size of $(57 \times 48)\mu\text{m}$ as shown in Fig. 1(c). Since the intensity of the injection laser was set to be significantly higher than that of the ionization laser, it could ionize more strongly bound electrons from argon and helium via tunneling ionization. The resulting localized plasma-density spike, calculated from the focus measurement with the ADK model [46], is shown in Fig. 1(d). The intensities of the ionization and injection lasers were set such that the former ionized argon up to its second level whilst the latter was capable of additionally ionizing the third ionization level of argon and the first of helium (see Table I). With such distinct gas ionization, it was possible to control the shape of the plasma, which initially followed the intensity distribution of the laser foci and was subsequently expected to expand hydrodynamically on the nanosecond timescale [47, 48].

Ion. level	Ion. energy (eV)	$I(W_{\text{ADK}}=1 \text{ fs}^{-1}) (\text{W/cm}^2)$
Ar-I	15.76	4.6×10^{14}
Ar-II	27.63	1.1×10^{15}
Ar-III	40.74	2.2×10^{15}
He-I	24.59	2.2×10^{15}
He-II	54.42	1.2×10^{16}

Table I. Relevant ionization energies [49] and the corresponding laser intensities for a tunnel ionization rate [46] of 1 fs^{-1} .

C. Alignment and synchronisation

The ionization laser, injection laser, electron beam and capillary were required to be accurately spatially aligned. Furthermore, the laser timing was required to be set such that ionization occurred shortly before the arrival of the electron drive beam. In order to minimize moving parts in the FLASH vacuum, the capillary and the upstream and downstream OTRs were statically mounted on one base plate and controlled in position and angle by a hexapod inside a separate vacuum chamber via a mechanical feedthrough [50]. Two aluminum-coated silica screens were used to align the system by imaging the optical transition radiation from the passing electron beam and light

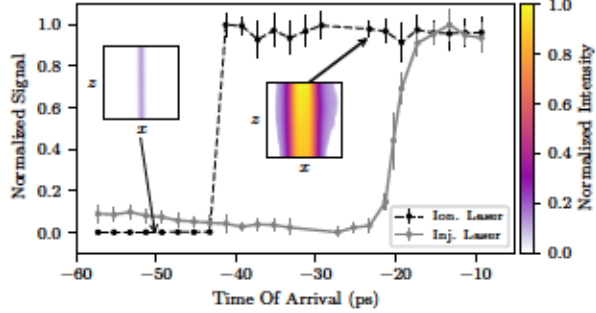


Figure 2. Normalized integrated plasma-afterglow signal as a function of the relative time of arrival (TOA) between the drive beam and the ionization (Ion.) and injection (Inj.) lasers; $t = 0$ is defined as the TOA of the electron beam. Inset are examples of the signal enhancement due to electron-beam-induced heating of the plasma formed by the ionization laser.

from the two lasers onto CCD cameras. These two reference points, 1.8 cm upstream of the capillary entrance and 27.4 cm downstream of the capillary exit, allowed for complete spatial overlap over the length of the plasma stage between the plasma generated by the ionization laser and the axis of the electron beam. The injection laser was aligned to the y -position of the electron-beam axis. The capillary was then moved such that each laser propagated through the appropriate channel in the capillary. Recent experimental results have shown that the recombination light from the plasma after the passage of an electron beam with currents of order kA can be used to synchronize lasers to electron beams to within a few femtoseconds [51]. This effect was used to synchronize the two laser arms to the drive beam. For this measurement, the plasma was ionized outside the capillary after filling the plasma chamber with argon gas to 0.05 mbar. Figure 2 shows the time-of-arrival (TOA) dependence of plasma light collected by a CCD camera viewing from the top for each of the laser arms; examples of camera images are depicted as insets. The visible transitions in Fig. 2 determine the time-of-arrival delay settings with respect to the electron beam of 42 ps for the ionization laser and 20 ps for the injection laser. Once the lasers were set up, the hexapod was positioned to maximise laser transmission through the capillary holes.

D. The electron drive beam

Downstream of the plasma, XQA quadrupoles [52] in combination with a spectrometer dipole and LANEX scintillating phosphor screens formed an imaging system capable of profiling electron beams from a few MeV to 2.4 GeV. Alternatively, the electron beam could be transported to an X-band transverse deflecting structure [53–55] for precise longitudinal-phase-space characterisation. The current profile of the drive beam, calculated from such a measurement, is shown in Fig. 1(e). Additionally,

the longitudinal phase space of the drive beam could be manipulated upstream of the plasma chamber with an energy collimator located in the dispersive section of the beamline [56]. The charge and position of the drive beam were measured at various locations along the beamline by toroidal current transformers (toroids) in combination with stripline and cavity BPMs [57]. The charge of the internally injected witness beam was determined in two independent ways: by subtracting the charges determined by a BPM directly downstream and a toroid upstream of the interaction point with a resolution of 1 pC [58]; and from a charge-calibrated phosphor screen in the electron spectrometer. A drive beam with a charge of (790 ± 4) pC was accelerated to (1116 ± 6) MeV and compressed to a peak current of 2.1 kA. The beam, with a transverse root-mean-squared (rms) normalized emittance of $\epsilon_{x,y} = (14.0 \times 5.3) \mu\text{m}$, was focused at the entrance of the capillary by four quadrupoles to a spot size of $\sigma_{x,y}^d = (25.5 \pm 1.6) \mu\text{m} \times (17.1 \pm 0.8) \mu\text{m}$, as measured by a transverse phase-space measurement using the combination of two BPMs and a scan of the spectrometer object plane [59]. The plateau plasma density was determined to be $1.4^{+0.4}_{-0.3} \times 10^{16} \text{ cm}^{-3}$ by comparing the measured and simulated energy losses of the drive beam, where the measured beam parameters, such as spot size, energy, current distribution and emittance were used as inputs to the simulation.

IV. PARTICLE-IN-CELL SIMULATIONS

The experiment was modeled with the 3D particle-in-cell (PIC) simulation code OSIRIS [60]. The modeled plasma-density distribution with a plateau density of $1.4 \times 10^{16} \text{ cm}^{-3}$ was derived from gas-density profiles, simulated with COMSOL and tunneling ionization calculations [46], based on the intensity distributions of the laser foci. Additionally, numerical studies with the code FBPIC [61] to model the pre-ionization showed that the longitudinal plasma-density profile beyond an acceleration length of 10 mm would develop a taper resulting from ionization defocussing. Such a taper can lead to a rephasing of the witness beam to lower accelerating fields. However, in this work, the discussion is limited to the injection process and the flat-top region; the longitudinal plasma-density profile that optimizes the acceleration to higher energies will be the subject of future work.

Simulations were conducted with a co-moving window of $(460 \times 400 \times 400) \mu\text{m}$ in (z, x, y) with $(256 \times 256 \times 256)$ cells. The drive-beam current profile, charge, and spot size were modeled based on the measurements described in Sec. III. The number of macro-particles per cell (PPC) for the drive beam was 8. While the PPC for the background plasma electrons was 1, the PPC was increased to 8 in a radius of $100 \mu\text{m}$ around the injection laser focus to resolve the physics of the injection process more accurately. The simulation case shown in this section represents the measurements shown in Figs. 5–8 as

well as the working point marked in Fig. 9.

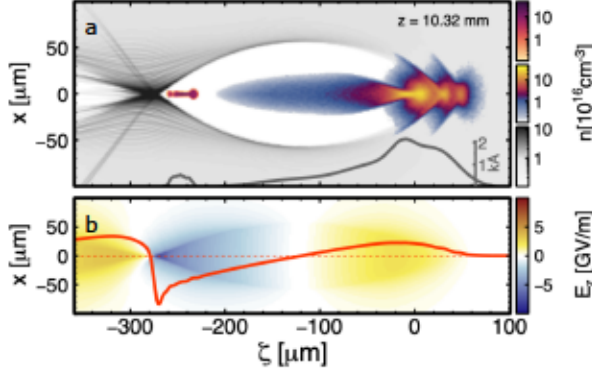


Figure 3. Simulation snapshot during the witness-beam acceleration: Cut through the plasma wake with electron densities (a) of witness beam (top right-hand colorbar), drive-beam (central colorbar), background plasma (bottom colorbar) and longitudinal current profile (solid gray line). (b) Longitudinal electric field as a central cut and an on-axis one-dimensional projection (solid red line).

The slice properties and longitudinal phase space of the witness beam are shown in Fig. 4. The simulated witness-beam charge is in excellent agreement with the measured values discussed in Sec. V.

As described in Sec. V, the injection laser was positioned $(23.5 \pm 4.5)\mu\text{m}$ off axis with respect to the electron beam for the majority of the data taking. The simulations show that such an offset leads to an increased emittance in the y direction compared to sub- μm emittance in x . In future experiments, this asymmetry can be avoided with wider transverse foci, enabling sub- μm emittance beams in both planes, as predicted for similar parameters [36].

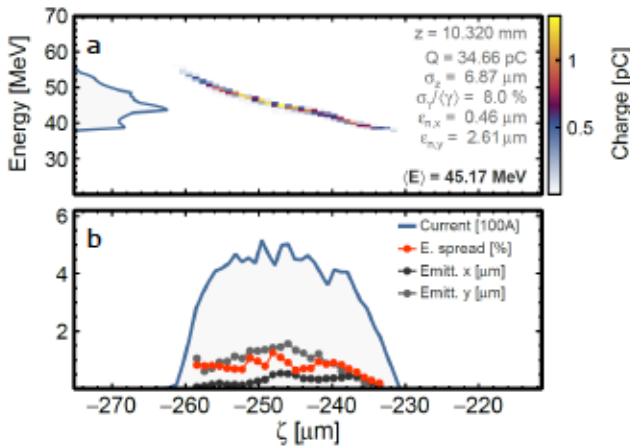


Figure 4. Longitudinal phase space of the simulated witness-beam parameter (a) and slice parameters (b) after 10.32 mm of acceleration.

Figure 4 shows that the simulated witness beam has a strongly correlated energy spread. While relatively large

energy spread is a characteristic but undesirable property of electron beams from many plasma accelerators, a linearly correlated longitudinal phase space such as that shown in Fig. 4(a) can be corrected for in a downstream plasma dechirper stage [8–10, 62] or by overloading the plasma wake with additionally injected charge [63].

V. EXPERIMENTAL RESULTS

A. Laser-controlled injection

The first investigation explored how the witness beams depended on the presence of the injection laser. This is shown in Fig. 5. Panel (a) depicts the energy spectrum of the witness beam over 500 consecutive shots at a spectrometer imaging energy of 45 MeV, while the corresponding excess-charge values are plotted in panel (b). The injection laser was blocked and unblocked for 100 shots at a time. There is a 100% correlation between the existence of a witness beam and the presence of the injection laser, with no entries being outside the range of the plot. The excess charge was $Q_{\text{on}} = (32.1 \pm 9.6)\text{ pC}$ when the injection laser was switched on and $Q_{\text{off}} = (0 \pm 5)\text{ pC}$ otherwise. The injection process is therefore unambiguously triggered by the injection laser. Furthermore, the data confirm that there is no contribution from the ionization laser, in agreement with the PIC simulations (see Sec. IV), so that downramp injection is established as the sole mechanism for witness-beam generation.

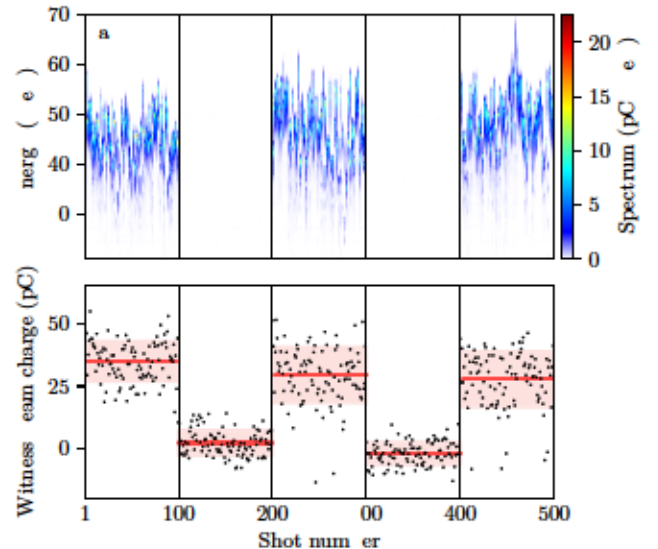


Figure 5. (a) Energy spectra and (b) charge of the injected witness beam. The injection is switched off by inserting a beam block inside the injection-laser path for shot numbers 101–200 and 301–400. The mean value for each group of 100 shots is indicated by a solid line, while the rms variation of charge values is shown by a shaded area.

B. Stability of witness-beam parameters

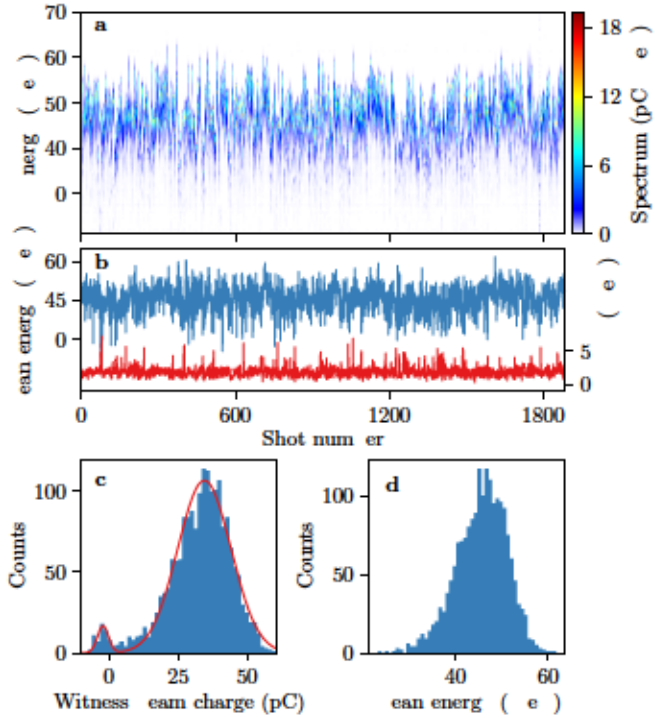


Figure 6. (a) Waterfall plot of the witness-beam spectrum for 1,885 consecutive shots. (b) The electron-beam mean energy (blue) and rms energy spread (red). (c) Histogram of the witness-beam charge, measured from the calibrated spectrometer screen with a double-Gaussian fit shown in red. (d) Histogram of the witness beam mean energy. Each histogram has 50 bins.

A dataset of 1,885 consecutive shots taken at a repetition rate of 2 Hz and recorded over a time span of approximately 15 minutes was used to explore the reliability of the plasma cathode. A waterfall plot of the projected witness-beam energy spectra is shown in Fig. 6(a). The spectra are remarkably stable. Fig. 6(b) shows the evolution of the mean energy and rms energy spread. An injected witness beam was measured for $(95.4 \pm 2.5)\%$ of the shots presented in Fig. 6(a). The witness beam had a mean charge of (33 ± 10) pC and mean energy of (45 ± 5) MeV with an rms relative energy spread of $\langle \delta E/E \rangle = 4.4\%$.

C. Witness-beam emittance and divergence

In the absence of focusing forces, a witness beam with a mean Lorentz factor $\langle \gamma \rangle$, transverse normalized emittance ε_x^n , and a beta function β^* at its virtual source point s_0 will expand outside the plasma such that it has

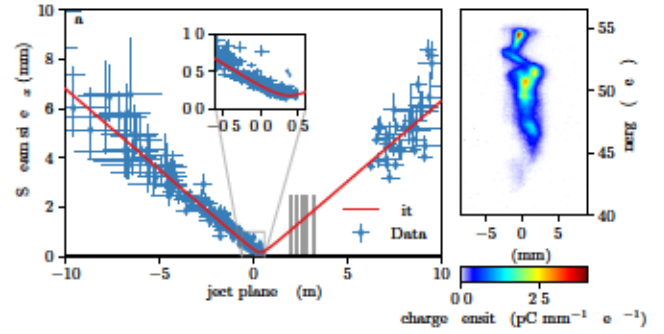


Figure 7. (a) Scan of the imaging quadrupole focusing strength. Each data point represents a single shot with an injected witness beam. Transverse beam sizes on the spectrometer screen and mean Lorentz factor $\langle \gamma \rangle$ were calculated from the spectrometer signal. From the quadrupole strength and $\langle \gamma \rangle$, the object plane s and the magnification were calculated to extract $\sigma_x(s)$ at the corresponding object plane. Error bars on σ_x and s were calculated analogously based on the rms-variation of the witness-beam spectral projection. The exit of the capillary is at $s = 0$. Object planes in the range between $s = 0.2$ m – 5.9 m lie too close to the quadrupoles (shown as gray lines) to be imaged. (b) An example of a witness-beam signal as measured on the spectrometer screen.

a transverse rms beam size of

$$\sigma_x(s) = \sqrt{\frac{\varepsilon_x^n}{\langle \gamma \rangle} \left(\beta^* + \frac{(s - s_0)^2}{\beta^*} \right)}. \quad (2)$$

at longitudinal position s .

Due to the stability of the injection process, this free-space propagation can be examined in a multi-shot measurement by imaging witness beams from different object-plane positions, s . Figure 7(a) shows the results of a scan of the quadrupole focusing strength of the imaging spectrometer, giving transverse beam size at the corresponding object plane, which gives information about the transverse expansion of the beam. Fitting Eq. 2 to the data gives a divergence of $\theta = (0.65 \pm 0.01)$ mrad, $s_0 = (381 \pm 6)$ mm, and a transverse rms normalized emittance projected over all shots of $\varepsilon_x^n = (9.3 \pm 0.3)$ μm . The fact that s_0 appears to be downstream of the capillary exit is probably an effect of the gas-density transition between the exit of the capillary and the vacuum of the plasma chamber. According to hydrodynamic simulations, gas-density ramps with atomic densities of order 10^{14} cm^{-3} can extend over tens of centimeters. This gas would be ionized by the ionization laser due to its long Rayleigh length. Plasma wakes driven in such a low-density plasma would continue to focus the witness beam for several centimeters beyond the capillary, possibly explaining the particularly low divergence.

An example of the witness-beam signal measured on the spectrometer screen is shown in Fig. 7(b). Since the longitudinal phase space of a witness beam in a plasma accelerator is typically predominantly linear (see

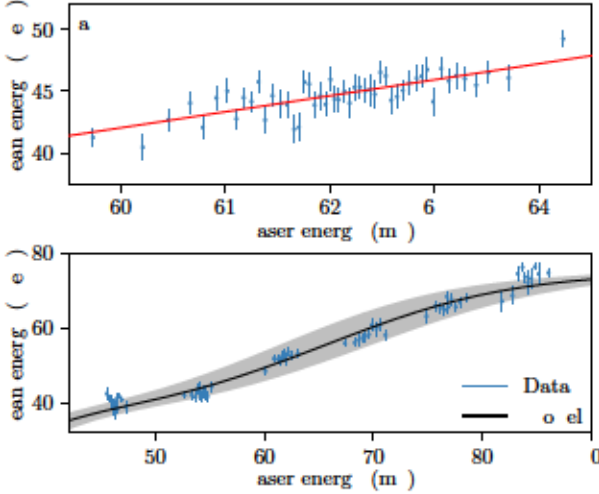


Figure 8. (a) Correlation between witness beam energy and total laser energy for the dataset shown in Fig. 6(a). The line is the result of a straight-line fit to the data points. (b) Results from a laser energy scan, highlighting the variation of witness-beam energy with on-target laser energy. The solid line is a fit based on the model of Eq. 3; the gray area marks the uncertainty of the model caused by the pulse-length jitter.

Sec. IV), the visible oscillatory structure can be interpreted as transverse centroid oscillations of longitudinal witness-beam slices. This is likely to contribute to the relatively high measured emittance compared to predicted values from numerical studies.

D. Influence of laser energy on the plasma cathode

Understanding the influences on the witness-beam characteristics is of primary importance in controlling the injection process whilst optimising its stability, a prerequisite for a reliable electron-beam source. As the plasma is laser ionized, variations in laser-pulse properties are important. No dependence of the charge or energy of the witness beam on laser timing was detected up to at least ≈ 200 ps relative time-of-arrival between the drive-beam and the laser pulses. The ionization and the injection laser arms were derived from the same laser system, so the inherent laser-energy jitter may affect both the longitudinal and transverse laser ionization and thus the shape of both plasmas. The effect of the laser energy stability on the witness-beam energy was studied by examining the dataset of 1,885 consecutive shots on which Fig. 6 was based. The variation of mean witness-beam energy as a function of on-target laser energy is plotted in Fig. 8(a). The observed linear correlation shows that the witness-beam energy jitter will depend on the stability of the laser energy. This relationship is illustrated more clearly by systematically varying the injection-laser energy over a much larger range, between 45 mJ and 86 mJ. The data is shown in Fig. 8(b). In

the fit, a model is used which is based on the fact that higher plasma densities lead to higher accelerating fields and consequently to higher witness-beam energies. Since the plasma-density changes are relatively small in this energy range, the accelerating field acting upon the witness beam E_{acc} was assumed to be proportional to the wave-breaking field $E_{\text{WB}} = c \sqrt{\frac{n_e m_e}{\epsilon_0}}$ [64]. The witness-beam energy $\mathcal{E} = e L_{\text{acc}} E_{\text{acc}}$ can be parametrized as

$$\mathcal{E} = \eta e L_{\text{acc}} E_{\text{WB}} = \eta e L_{\text{acc}} c \sqrt{\frac{m_e}{\epsilon_0} [n_e(U_{\text{laser}}) + n_{\text{offset}}]}, \quad (3)$$

where U_{laser} is the on-target laser energy, η is a constant adjusting for deviations in effective acceleration length and deviations from acceleration at wave-breaking field-strength and n_{offset} describes an offset in effective average plasma density. The values of $n_e(U_{\text{laser}})$ were calculated numerically using the ADK model [46], assuming that the laser pulse length and spot size were constant inside the plasma.

The success of this model is illustrated in Fig. 8(b), showing that the change in the mean energy of the witness beam with the total laser energy can be understood as an increase in the average plasma density due to additional Ar-II ionization at higher laser energies. The fit to the data results in $n_{\text{offset}} = (-65.5 \pm 1.7) \times 10^{14} \text{ cm}^{-3}$ and $\eta = 0.206 \pm 0.002$, indicating that the witness beam experiences a lower average plasma density than expected for a uniform longitudinal plasma profile and acceleration at a non-ideal phase or reduced acceleration length. These findings can be explained, for example, with a tapered longitudinal profile caused by ionization defocussing as discussed in Section IV.

The laser rms energy jitter was measured to be 1.5 %. The slope extracted from the model described above translates this into an rms energy jitter of the witness beam of 3.9 %. This is sufficiently small that the accelerating field can be fine-tuned between 1.3 and 2.7 GV/m by varying the laser energy. Control can be improved further by either designing laser systems with lower energy jitter or by using different gas mixtures. For example, if the argon in the gas mixture were to be replaced with hydrogen, the ionization stemming from the ionization laser can saturate, reducing the sensitivity to the laser energy.

E. Influence of the injection laser position on the plasma cathode

That precise alignment between the two laser arms and the electron beam is crucial to stable injection can be seen in Fig. 9, which shows the effect on the injected witness charge of changing the height of the injection laser with respect to the electron-beam axis. The height was changed by moving the optical assembly of the injection laser in the y -direction along the laser-beam path such that the alignment with respect to the off-axis parabola

remained unchanged. The relative calibration between focus position and motor position was carried out with the upstream OTR camera.

Every data point plotted in Fig. 9 represents the average of 20 events; the error on the measured charge is given by the rms variation of the witness-beam charge. The positioning error bar, $\sigma_y^{e,\text{inj}} = 4.5 \mu\text{m}$, was constant throughout the dataset and was calculated from two main contributions: the rms y -position jitter of the electron beam at the injection position, $\sigma_y^e = 1.4 \mu\text{m}$, measured by two cavity BPMs [57] around the plasma chamber; and the rms variation of the laser centroid y position, $\sigma_y^{\text{inj}} = 4.2 \mu\text{m}$, measured at the focus. The influence of the jitter on the z position of the injection laser, $\sigma_z^{\text{inj}} = 3.4 \mu\text{m}$ was neglected, as it led to a difference in longitudinal injection position that made a negligible contribution to the witness-beam energy jitter. Furthermore, the x -position jitter of the electron-beam waist, $\sigma_x^e = 1.0 \mu\text{m}$ was also assumed to have a negligible effect, since it was much smaller than the Rayleigh length of the injection-laser focus. The scan was only performed on one side of the injection-laser position distribution.

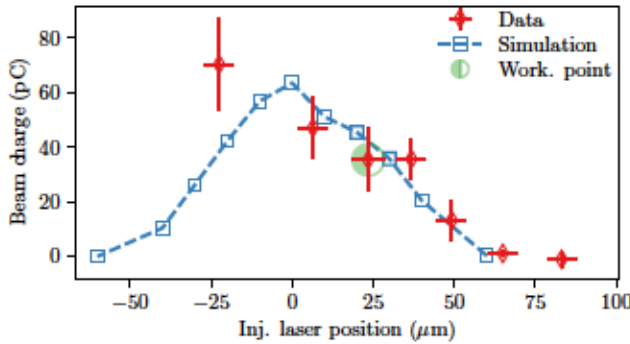


Figure 9. Effect of centroid laser-spot positioning with respect to the electron beam. The laser position was measured on the upstream OTR camera and the charge on the electron spectrometer screen (points with error bars). Results are compared to simulation results, shown as squares (for details see Sec. IV), with the plasma profile modeled as shown in Fig. 1(d). The working point for the data presented in this paper is indicated by the half-filled circle.

A comparison between the experimental data and a simulated offset scan is plotted in Fig. 9, based on the measured plasma profile (see Fig. 1(d)). In this Figure, zero is at the highest simulated injected charge. Since the relative offset between the electron beam and injection laser was not measured to sub-spot-size accuracy, it was determined by fitting the simulation-based model to the data. The data presented in Figs. 5 - 8 were taken at the point indicated in Fig. 9 as the “work. point”, which shows lower sensitivity to the relative alignment than the experimentally determined position of maximum charge at $y = (-22.5 \pm 4.5) \mu\text{m}$. The slope of the simulation-

based model gives an estimate of the charge variation resulting from position jitter, $\delta Q_{\text{wit.}}(\sigma_y^{e,\text{inj}}) = 6.9 \text{ pC}$. The charge variation in the witness bunch can be explained predominantly by the position jitter between the electron beam and the injection laser, which is known to be dominated by the laser pointing jitter. This jitter would be eliminated by using an injection laser with a spot size that is many times wider than the plasma wake. Such a shape can be produced with focusing optics that produce asymmetric foci, such as cylindrical lenses.

VI. SUMMARY

A plasma cathode with stability at a level unprecedented in the field of beam-driven plasma injectors has been demonstrated, studied, and operated reliably. Effective accelerating gradients of GV/m were demonstrated, tunable in the range of 1.3 – 2.7 GV/m. The stability allowed a multi-shot measurement of the beam-divergence and emittance to be performed. Sources of charge and energy jitter were identified and mitigation strategies were proposed for future applications. Particle-in-cell simulations gave good agreement with the observed witness-beam parameters. These indicate that the requirements for future compact FELs of sub-micron emittances in both planes, peak currents of a few hundred amperes and narrow energy spread can be attained using the methods described in this paper. These results constitute a significant step towards stable, controllable plasma-based cathodes and brightness converter stages, which are of great interest for next-generation photon-science and particle-physics facilities.

ACKNOWLEDGMENTS

The authors would like to thank M. Dinter, S. Karstensen, K. Ludwig, F. Marutzky, A. Rahali, V. Rybnikov, A. Schleiermacher and S. Thiele, as well as the FLASH accelerator team, DESY MVS and the DESY FH and M divisions for their engineering and technical support. We thank the OSIRIS consortium (IST/UCLA) for access to the OSIRIS code and acknowledge the use of the High-Performance Cluster (Maxwell) at DESY. We also gratefully acknowledge the Gauss Centre for Supercomputing e.V. (www.gauss-centre.eu) for funding this project by providing computing time through the John von Neumann Institute for Computing (NIC) on the GCS Supercomputer JUWELS at Jülich Supercomputing Centre (JSC). B.H. and L.B. were supported by the European Research Council (ERC) under the European Unions Horizon 2020 research and innovation programme (NeXsource, ERC Grant agreement No. 865877). We furthermore thank the developers of the pipeline-analysis software, Manuel Kirchen and Sören Jalas from the University of Hamburg.

-
- [1] J. B. Rosenzweig, D. B. Cline, B. Cole, H. Figueroa, W. Gai, R. Konecny, J. Norem, P. Schoessow, and J. Simpson, Experimental observation of plasma wakefield acceleration, *Phys. Rev. Lett.* **61**, 98 (1988).
- [2] P. Chen, J. M. Dawson, R. W. Huff, and T. Katsouleas, Acceleration of electrons by the interaction of a bunched electron beam with a plasma, *Phys. Rev. Lett.* **54**, 693 (1985).
- [3] J. B. J. B. Rosenzweig, B. Breizman, T. Katsouleas, and J. J. Su, Acceleration and focusing of electrons in two-dimensional nonlinear plasma wake fields, *Phys. Rev. A* **44**, R6189 (1991).
- [4] T. Tajima and J. M. Dawson, Laser electron accelerator, *Phys. Rev. Lett.* **43**, 267 (1979).
- [5] R. D. Ruth, A. W. Chao, L. Morton, and P. B. Wilson, A Plasma Wake Field Accelerator, *Part. Accel.* **17**, 171 (1985).
- [6] B. Cros, P. Muggli, C. Schroeder, S. Hooker, P. Piot, J. England, S. Gessner, J. Vieira, E. Gschwendtner, J.-L. Vay, *et al.*, Towards an Advanced Linear International Collider ALEGRO collaboration, *arXiv* (2019).
- [7] I. Blumenfeld, C. E. Clayton, F. J. Decker, M. J. Hogan, C. Huang, R. Ischebeck, R. Iverson, C. Joshi, T. Katsouleas, N. Kirby, *et al.*, Energy doubling of 42 GeV electrons in a metre-scale plasma wakefield accelerator, *Nature* **445**, 741 (2007).
- [8] R. D'Arcy, S. Wesch, A. Aschikhin, S. Bohlen, C. Behrens, M. J. Garland, L. Goldberg, P. Gonzalez, A. Knetsch, V. Libov, *et al.*, Tunable Plasma-Based Energy Dechirper, *Phys. Rev. Lett.* **122**, 034801 (2019).
- [9] V. Shpakov, M. P. Anania, M. Bellaveglia, A. Biamoni, F. Bisesto, F. Cardelli, M. Cesarini, E. Chiadroni, A. Cianchi, G. Costa, *et al.*, Longitudinal Phase-Space Manipulation with Beam-Driven Plasma Wakefields, *Phys. Rev. Lett.* **122**, 114801 (2019).
- [10] Y. P. Wu, J. F. Hua, Z. Zhou, J. Zhang, S. Liu, B. Peng, Y. Fang, Z. Nie, X. N. Ning, C.-H. Pai, *et al.*, Phase space dynamics of a plasma wakefield dechirper for energy spread reduction, *Phys. Rev. Lett.* **122**, 204804 (2019).
- [11] M. Litos, E. Adli, W. An, C. I. Clarke, C. E. Clayton, S. Corde, J. P. Delahaye, R. J. England, A. S. Fisher, J. Frederico, *et al.*, High-efficiency acceleration of an electron beam in a plasma wakefield accelerator, *Nature* **515**, 92 (2014).
- [12] G. Loisch, G. Asova, P. Boonpornprasert, R. Brinkmann, Y. Chen, J. Engel, J. Good, M. Gross, F. Grüner, H. Huck, *et al.*, Observation of High Transformer Ratio Plasma Wakefield Acceleration, *Phys. Rev. Lett.* **121**, 064801 (2018).
- [13] S. Corde, E. Adli, J. M. Allen, W. An, C. I. Clarke, C. E. Clayton, J. P. Delahaye, J. Frederico, S. Gessner, S. Z. Green, *et al.*, Multi-gigaelectronvolt acceleration of positrons in a self-loaded plasma wakefield, *Nature* **524**, 442445 (2015).
- [14] V. Libov, A. Aschikhin, J. Dale, R. D'Arcy, K. Ludwig, A. Martinez de la Ossa, T. Mehrling, J. H. Roeckemann, L. Schaper, B. Schmidt, *et al.*, FLASHForward X-2: Towards beam quality preservation in a plasma booster, *Nuclear Instruments and Methods in Physics Research, Section A: Accelerators, Spectrometers, Detectors and Associated Equipment* **909**, 80 (2018).
- [15] C. Joshi, E. Adli, W. An, C. E. Clayton, S. Corde, S. Gessner, M. J. Hogan, M. Litos, W. Lu, K. Marsh, *et al.*, Plasma wakefield acceleration experiments at FACET II, *Plasma Phys. Control. Fusion* **60**, 034001 (2018).
- [16] B. Hidding, G. Pretzler, J. B. Rosenzweig, T. Königstein, D. Schiller, and D. L. Bruhwiler, Ultracold Electron Bunch Generation via Plasma Photocathode Emission and Acceleration in a Beam-Driven Plasma Blowout, *Phys. Rev. Lett.* **108**, 35001 (2012).
- [17] F. Li, J. F. Hua, X. L. Xu, C. J. Zhang, L. X. Yan, Y. C. Du, W. H. Huang, H. B. Chen, C. X. Tang, W. Lu, *et al.*, Generating High-Brightness Electron Beams via Ionization Injection by Transverse Colliding Lasers in a Plasma-Wakefield Accelerator, *Phys. Rev. Lett.* **111**, 15003 (2013).
- [18] A. Martinez de la Ossa, J. Grebenyuk, T. Mehrling, L. Schaper, and J. Osterhoff, High-quality electron beams from beam-driven plasma accelerators by wakefield-induced ionization injection, *Phys. Rev. Lett.* **111**, 245003 (2013).
- [19] N. Vafaei-Najafabadi, K. A. Marsh, C. E. Clayton, W. An, W. B. Mori, C. Joshi, W. Lu, E. Adli, S. Corde, M. Litos, *et al.*, Beam Loading by Distributed Injection of Electrons in a Plasma Wakefield Accelerator, *Phys. Rev. Lett.* **112**, 25001 (2014).
- [20] A. Deng, O. S. Karger, T. Heinemann, A. Knetsch, P. Scherkl, G. G. Manahan, A. Beaton, D. Ullmann, G. Wittig, A. F. Habib, *et al.*, Generation and acceleration of electron bunches from a plasma photocathode, *Nat. Phys.* **15**, 11561160 (2019).
- [21] E. Oz, S. Deng, T. Katsouleas, P. Muggli, C. D. Barnes, I. Blumenfeld, F. J. Decker, P. Emma, M. J. Hogan, R. Ischebeck, *et al.*, Ionization-induced electron trapping in ultrarelativistic plasma wakes, *Phys. Rev. Lett.* **98**, 084801 (2007).
- [22] A. Aschikhin, C. Behrens, S. Bohlen, J. Dale, N. Delbos, L. di Lucchio, E. Elsen, J.-H. Erbe, M. Felber, B. Foster, *et al.*, The FLASHForward facility at DESY, *Nuclear Instruments and Methods in Physics Research Section A: Accelerators, Spectrometers, Detectors and Associated Equipment* **806**, 175 (2016).
- [23] R. D'Arcy, A. Aschikhin, S. Bohlen, G. Boyle, T. Brümmel, J. Chappell, S. Diederichs, B. Foster, M. J. Garland, L. Goldberg, *et al.*, FLASHForward: Plasma wakefield accelerator science for high-average-power applications, *Philosophical Transactions of the Royal Society A: Mathematical, Physical and Engineering Sciences* **377**, 20180392 (2019).
- [24] W. Ackermann, G. Asova, V. Ayvazyan, A. Azima, N. Baboi, J. Bähr, V. Balandin, B. Beutner, A. Brandt, A. Bolzmann, *et al.*, Operation of a free-electron laser from the extreme ultraviolet to the water window, *Nat. Photon.* **1**, 336 (2007).
- [25] S. Schreiber and B. Faatz, The free-electron laser FLASH, *High Power Laser Science and Engineering* **3**, e20 (2015).
- [26] S. Bulanov, N. Naumova, F. Pegoraro, and J. Sakai, Particle injection into the wave acceleration phase due to nonlinear wake wave breaking, *Phys. Rev. E* **58**, R5257

- (1998).
- [27] H. Suk, N. Barov, J. B. Rosenzweig, and E. Esarey, Plasma electron trapping and acceleration in a plasma wake field using a density transition, *Phys. Rev. Lett.* **86**, 1011 (2001).
 - [28] G. Wittig, O. Karger, A. Knetsch, Y. Xi, A. Deng, J. B. Rosenzweig, D. L. Bruhwiler, J. Smith, G. G. Manahan, Z. M. Sheng, *et al.*, Optical plasma torch electron bunch generation in plasma wakefield accelerators, *Phys. Rev. ST Accel. Beams* **18**, 081304 (2015).
 - [29] G. Wittig, O. S. Karger, A. Knetsch, Y. Xi, A. Deng, J. B. Rosenzweig, D. L. Bruhwiler, J. Smith, Z. M. Sheng, *et al.*, Electron beam manipulation, injection and acceleration in plasma wakefield accelerators by optically generated plasma density spikes, *Nuclear Instruments and Methods in Physics Research, Section A: Accelerators, Spectrometers, Detectors and Associated Equipment* **829**, 83 (2016).
 - [30] B. Hidding, G. G. Manahan, O. Karger, A. Knetsch, G. Wittig, D. A. Jaroszynski, Z. M. Sheng, Y. Xi, A. Deng, J. B. Rosenzweig, *et al.*, Ultrahigh brightness bunches from hybrid plasma accelerators as drivers of 5th generation light sources, *Journal of Physics B: Atomic, Molecular and Optical Physics* **47**, 234010 (2014).
 - [31] Y. Wan, C. J. Zhang, F. Li, Y. P. Wu, J. F. Hua, C. H. Pai, W. Lu, Y. Q. Gu, X. L. Xu, C. Joshi, and W. B. Mori, Colliding ionization injection in a plasma wakefield accelerator, *Plasma Phys. Control. Fusion* **58**, 034015 (2016).
 - [32] M. C. Thompson, J. B. Rosenzweig, and H. Suk, Plasma density transition trapping as a possible high-brightness electron beam source, *Phys. Rev. ST Accel. Beams* **7**, 011301 (2004).
 - [33] T. Katsouleas, Physical mechanisms in the plasma wakefield accelerator, *Phys. Rev. A* **33**, 2056 (1986).
 - [34] R. J. England, J. B. Rosenzweig, and N. Barov, Plasma electron fluid motion and wave breaking near a density transition, *Phys. Rev. E* **66**, 016501 (2002).
 - [35] J. Grebenyuk, A. M. de la Ossa, T. Mehrling, and J. Osterhoff, Beam-driven plasma-based acceleration of electrons with density down-ramp injection at FLASHForward, *Nuclear Instruments and Methods in Physics Research Section A: Accelerators, Spectrometers, Detectors and Associated Equipment* **740**, 246 (2014).
 - [36] A. Martinez de la Ossa, Z. Hu, M. J. V. Streeter, T. J. Mehrling, O. Kononenko, B. Sheeran, and J. Osterhoff, Optimizing density down-ramp injection for beam-driven plasma wakefield accelerators, *Phys. Rev. Accel. Beams* **20**, 091301 (2017).
 - [37] X. L. Xu, F. Li, W. An, T. N. Dalichaouch, P. Yu, W. Lu, C. Joshi, and W. B. Mori, High quality electron bunch generation using a longitudinal density-tailored plasma-based accelerator in the three-dimensional blowout regime, *Phys. Rev. Accel. Beams* **20**, 111303 (2017).
 - [38] C. Zhang, C.-K. Huang, K. A. Marsh, X. L. Xu, F. Li, M. Hogan, V. Yakimenko, S. Corde, W. B. Mori, and C. Joshi, Effect of fluctuations in the down ramp plasma source profile on the emittance and current profile of the self-injected beam in a plasma wakefield accelerator, *Phys. Rev. Accel. Beams* **22**, 111301 (2019).
 - [39] A. J. Gonsalves, K. Nakamura, C. Lin, D. Panasenko, S. Shiraishi, T. Sokollik, C. Benedetti, C. B. Schroeder, C. G. R. Geddes, J. Van Tilborg, *et al.*, Tunable laser plasma accelerator based on longitudinal density tailoring, *Nat. Phys.* **7**, 862 (2011).
 - [40] J. Faure, C. Rechatin, O. Lundh, L. Ammoura, and V. Malka, Injection and acceleration of quasimonoenergetic relativistic electron beams using density gradients at the edges of a plasma channel, *Physics of Plasmas* **17**, 083107 (2010).
 - [41] K. Schmid, A. Buck, C. M. S. Sears, J. M. Mikhailova, R. Tautz, D. Herrmann, M. Geissler, F. Krausz, and L. Veisz, Density-transition based electron injector for laser driven wakefield accelerators, *Phys. Rev. Spec. Top.-AC* **13**, 91301 (2010).
 - [42] A. J. Gonsalves, K. Nakamura, J. Daniels, C. Benedetti, C. Pieronek, T. C. De Raadt, S. Steinke, J. H. Bin, S. S. Bulanov, J. Van Tilborg, C. G. Geddes, C. B. Schroeder, C. Tóth, E. Esarey, K. Swanson, L. Fan-Chiang, G. Bagdasarov, *et al.*, Petawatt laser guiding and electron beam acceleration to 8 gev in a laser-heated capillary discharge waveguide, *Phys. Rev. Lett.* **122**, 084801 (2019).
 - [43] A. Butler, D. J. Spence, and S. M. Hooker, Guiding of high-intensity laser pulses with a hydrogen-filled capillary discharge waveguide, *Phys. Rev. Lett.* **89**, 185003 (2002).
 - [44] E. Dickinson, H. Ekstroem, and E. Fontes, COMSOL Multiphysics: Finite element software for electrochemical analysis. A mini-review, *Electrochemistry communications* **40**, 71 (2014).
 - [45] S. Schulz, I. Grguraš, C. Behrens, H. Bromberger, J. T. Costello, M. K. Czwalinna, M. Felber, M. C. Hoffmann, M. Ilchen, H. Y. Liu, and others, Femtosecond all-optical synchronization of an X-ray free-electron laser, *Nat. Commun.* **6** (2015).
 - [46] M. V. Ammosov, N. B. Delone, and V. Krainov, Tunnel ionization of complex atoms and of atomic ions in an alternating electric field, *Sov. Phys. JETP* **64**, 1191 (1986).
 - [47] C. G. Durfee and H. M. Milchberg, Light pipe for high intensity laser pulses, *Phys. Rev. Lett.* **71**, 2409 (1993).
 - [48] R. J. Shalloo, C. Arran, L. Corner, J. Holloway, J. Jonnerby, R. Walczak, H. M. Milchberg, and S. M. Hooker, Hydrodynamic optical-field-ionized plasma channels, *Phys. Rev. E* **97**, 053203 (2018).
 - [49] NIST Atomic Spectra Database Ionization Energies (2020).
 - [50] D. John, O. Jens, S. Lucas, and L. Kai, *Vorrichtung Mit Beweglicher Aufnahme Für Vakuumkammern* (2014).
 - [51] P. Scherkl, A. Knetsch, T. Heinemann, A. Sutherland, A. F. Habib, O. Karger, D. Ullmann, A. Beaton, G. Kirwan, G. Manahan, *et al.*, Plasma-photonic spatiotemporal synchronization of relativistic electron and laser beams, *arXiv* (2019).
 - [52] I. Okunev, I. Morozov, and N. Nefedov, X-FEL Quadrupole with Gradient of 100 T/m, *Physics Procedia* **84**, 101 (2016).
 - [53] B. Marchetti, R. Assmann, B. Beutner, J. Branlard, F. Christie, R. D'Arcy, W. Decking, U. Dorda, J. Herrmann, *et al.*, X-Band TDS Project, in *Proc. IPAC17* (Copenhagen, 2017) pp. 184–187.
 - [54] R. D'Arcy, A. Aschikhin, P. Gonzalez Caminal, V. Libov, and J. Osterhoff, Longitudinal Phase Space Reconstruction at FLASHForward Using a Novel X-Band Transverse Deflection Cavity, PolariX, in *9th International Particle Accelerator Conference* (2018).
 - [55] R. D'Arcy, V. Libov, and J. Osterhoff, A transverse deflecting structure for the plasma wakefield accelerator experiment, FLASHForward, in *IBIC'16* (JACOW,

- Barcelona, 2016) pp. 760–763.
- [56] S. Schröder, K. Ludwig, A. Aschikhin, R. D’Arcy, M. Dinter, P. Gonzalez, S. Karstensen, A. Knetsch, V. Libov, C. A. Lindstrøm, *et al.*, Tunable and precise two-bunch generation at FLASHForward, *arXiv* (2020).
- [57] D. Lipka, D. Nölle, M. Siemens, and S. Vilcins, Development of cavity BPM for the european XFEL, in *Proceedings of LINAC* (Tsukuba, 2010).
- [58] D. Lipka, A. Affeldt, R. Awwad, N. Baboi, R. Barret, B. Beutner, F. Brinker, W. Decking, A. Delfs, M. Drewitsch, *et al.*, First experience with the standard diagnostics at the European XFEL injector, in *IBIC’16* (Barcelona, 2016) pp. 14–19.
- [59] C. A. Lindstrøm, R. D’Arcy, M. J. Garland, P. Gonzalez, B. Schmidt, S. Schröder, S. Wesch, and J. Osterhoff, Matching small β functions using centroid jitter and two beam position monitors, *Phys. Rev. Accel. Beams* **23**, 052802 (2020).
- [60] R. A. Fonseca, L. O. Silva, F. S. Tsung, V. K. Decyk, W. Lu, C. Ren, W. B. Mori, S. Deng, S. Lee, T. Kat-souleas, and J. C. Adam, OSIRIS: A three-dimensional, fully relativistic particle in cell code for modeling plasma based accelerators, in *International Conference on Computational Science* (Springer, Berlin, 2002) pp. 342–351.
- [61] R. Lehe, M. Kirchen, I. A. Andriyash, B. B. Godfrey, and J. L. Vay, A spectral, quasi-cylindrical and dispersion-free Particle-In-Cell algorithm, *Comput. Phys. Commun.* **203**, 66 (2016).
- [62] A. Ferran Pousa, A. Martinez de la Ossa, R. Brinkmann, and R. W. Assmann, Compact multistage plasma-based accelerator design for correlated energy spread compensation, *Phys. Rev. Lett.* **123**, 054801 (2019).
- [63] G. G. Manahan, A. F. Habib, P. Scherkl, P. Delinikolas, A. Beaton, A. Knetsch, O. Karger, G. Wittig, T. Heinemann, Z.-M. Sheng, *et al.*, Ultrahigh 6D-brightness electron beams: single-stage plasma-based correlated energy spread compensation, *Nat. Commun.* **8** (2017).
- [64] J. M. Dawson, Nonlinear Electron Oscillations in a Cold Plasma, *Phys. Rev.* **113**, 383 (1959).